ACS APPLIED MATERIALS & INTERFACES

Research Article

www.acsami.org

High-Flux Oxygen-Transporting Membrane $Pr_{0.6}Sr_{0.4}Co_{0.5}Fe_{0.5}O_{3-\delta}$: CO_2 Stability and Microstructure

Kaveh Partovi,* Fangyi Liang, Olga Ravkina, and Jürgen Caro

Institute of Physical Chemistry and Electrochemistry, Leibniz University Hannover, Callinstraße 3A, D-30167 Hannover, Germany

ABSTRACT: High oxygen permeability and good thermochemical stability of oxygen-transporting membranes (OTMs) are two main requirements concerning the applicability of these devices in chemical processes, such as CO_2 capture using the oxyfuel concept or catalytic membrane reactors. In this work, a single-phase perovskite-type membrane $Pr_{0.6}Sr_{0.4}Co_{0.5}Fe_{0.5}O_{3-\delta}$ (PSCF) with 0.6-mm thickness was subjected to periodic thermal cycling in the temperature range between 850 and 1000 °C in a 1000-h long-term permeation test with pure CO_2 as the sweep gas. The results of this long-term permeation operation revealed a stepwise increase in oxygen permeation values at 1000 °C after each thermal cycle, reaching from 1.38 cm^3 (STP) min^{-1} cm^{-2} in the first cycle to 1.75 cm^3 (STP) min^{-1} cm^{-2} in the fourth cycle. Furthermore, the membrane showed very good CO_2 stability at 900 °C and above. Despite a partial decrease in oxygen permeation fluxes at 850 °C, a steady state of 0.25 cm^3 (STP) min^{-1} cm^{-2} was reached and maintained for more than 100 h. The newly developed PSCF membrane also exhibited a higher oxygen permeation flux with He and CO_2 sweeping at all measured temperatures compared to a similar $La_{0.6}Sr_{0.4}Co_{0.8}Fe_{0.2}O_{3-\delta}$ (LSCF) membrane.

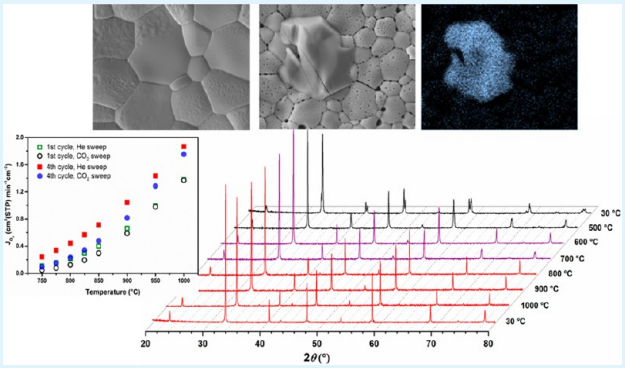

KEYWORDS: *CO_2-stable membrane, perovskite, mixed conductor, oxygen permeation, long-term stability, phase transition*

1. INTRODUCTION

Mixed ionic−electronic conducting (MIEC) ceramic oxides have gained considerable attention, because of their wide variety of potential applications as oxygen-transporting membranes (OTMs) in energy industries and petrochemical processes involving oxygen separation at high temperatures.[1] Some examples include utilization of OTMs as oxygen suppliers and distributors in processes such as oxidative coupling of methane to ethylene and ethane (OCM)[2−4] and partial oxidation of methane (POM) to syngas (CO + H_2)[5−7] or as cathode materials for solid oxide fuel cells (SOFCs).[8,9] Furthermore, OTMs have recently received more attention as potential oxygen suppliers for CO_2 capture through an oxyfuel route in power plants.[10−12]

Among perovskite-type mixed oxides, the highest values of oxygen permeation flux have been observed for the compositions containing alkaline-earth metal ions (especially Ba^{2+} and Sr^{2+}) on the A site of their ABO_3 structures.[13,14] However, in the presence of notable concentrations of CO_2 on the feed or permeate side of the membrane, formation of a continuous layer of alkaline-earth carbonate on the membrane's surface hinders the oxygen exchange reaction, resulting in a dramatic drop of the oxygen flux to a negligible level.[15−18] Therefore, the CO_2 tolerance of an OTM is of crucial importance for its applicability in chemical processes involving CO_2, such as the oxyfuel concept.

One strategy to obtain CO_2-stable membranes is to develop perovskite or perovskite-like materials completely free of alkaline-earth metals as single-phase or as mixed-matrix membranes. However, the oxygen permeability of these materials is very low for practical applications.[12,19] Another approach is the enhancement of the membrane's CO_2 stability by partial substitution of the cations in the A and/or B sites with elements that are less reactive toward CO_2, thus preserving the perovskite structure against carbonate formation at the cost of lower permeation levels. For example, it was reported that the CO_2 tolerance in $SrCo_{0.8}Fe_{0.2}O_{3-\delta}$ could be improved by replacing 10% of the cobalt and iron in the B site by tantalum[20] or titanium.[21]

Furthermore, the concept of replacing higher contents of alkaline-earth elements in the A site with rare-earth cations has been developed. Rare-earth cations are similar in size to alkaline-earth cations, but their their carbonates decompose at lower temperatures.[22] As an example, the A site of calcium- and strontium-containing perovskites was partially exchanged with the rare-earth element lanthanum.[23,24] Evaluation of the collective data regarding the thermodynamic stabilities of carbonates under different CO_2 partial pressures, provided as an Ellingham diagram,[23] predicted a decomposition temper-

Received: March 20, 2014
Accepted: June 5, 2014
Published: June 5, 2014

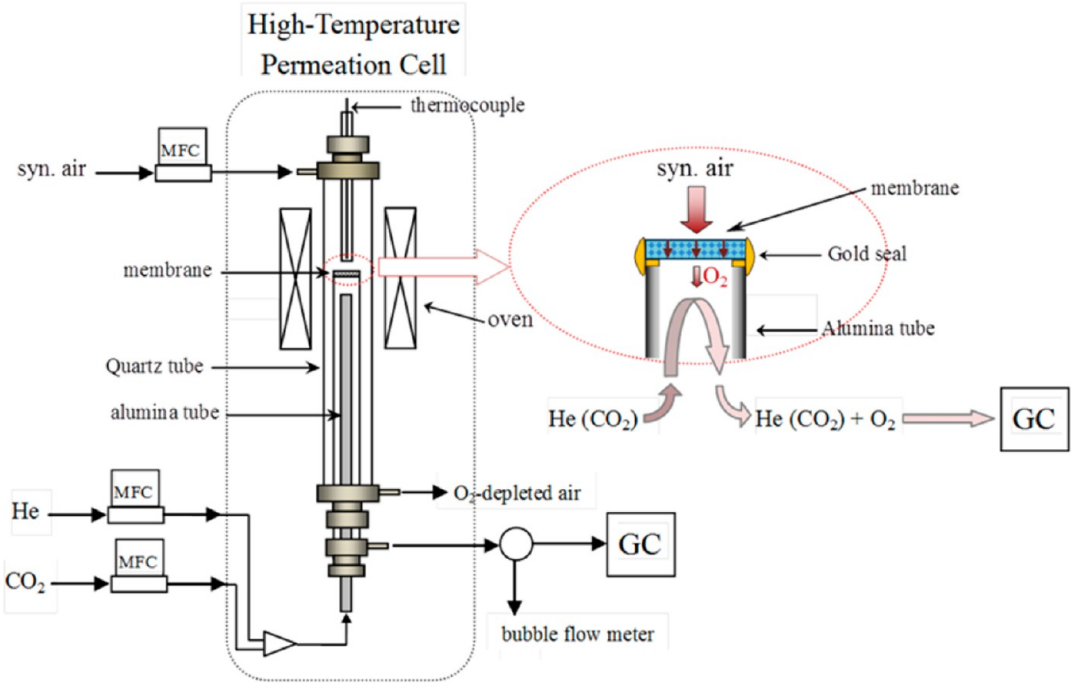

Figure 1. Schematic drawing of the experimental setup for oxygen permeation measurements.

ature of >1100 °C for pure $SrCO_3$ under an atmospheric pressure of CO_2. However, according to studies by Yokokawa et al.,[25] in the case of perovskite mixed oxides, the stabilization energy of the perovskite should also be taken into consideration. In other words, large negative stabilization energies of the perovskite oxide in Sr-containing perovskite structures result in higher stability against $SrCO_3$ formation. However, despite their acceptable tolerance in long-term oxygen permeation experiments under CO_2-containing atmospheres, the oxygen fluxes of these materials are relatively low, because of the higher-valence state of La^{3+} in comparison with Sr^{2+}, which results in a lower concentration of oxygen vacancies. Furthermore, the smaller size of La^{3+}(XII) (r = 136 pm)[26] compared to Sr^{2+}(XII) (r = 144 pm)[26] results in reduced lattice parameters and, therefore, leads to a decreased oxygen flux. To compensate this deficit of low oxygen flux, surface-rich hollow fibers of $La_{0.6}Sr_{0.4}Co_{0.8}Fe_{0.2}O_{3-\delta}$ have been developed.[27]

Perovskite-type strontium cobaltite with A-site Pr substitution ($Pr_{0.6}Sr_{0.4}CoO_{3-\delta}$) was introduced by an early work of Teraoka et al.[28] In a more recent work, Serra et al. studied the system $A_{0.68}Sr_{0.3}Fe_{0.8}Co_{0.2}O_{3-\delta}$ (where A represents rare-earth metals and Ba) as cathode materials.[29] Also, in previous works by our group, we developed two dual-phase membranes containing perovskites with A-site Pr substitution as the mixed conducting phase, such as $Ce_{0.9}Pr_{0.1}O_{2-\delta}$–$Pr_{0.6}Sr_{0.4}FeO_{3-\delta}$ (CP–PSF)[30] and $Ce_{0.9}Pr_{0.1}O_{2-\delta}$–$Pr_{0.6}Sr_{0.4}Fe_{0.5}Co_{0.5}O_{3-\delta}$ (CP–PSFC),[31] that show high oxygen permeability and good chemical stability in a CO_2 atmosphere at high temperatures. In this paper, we describe a new perovskite material, $Pr_{0.6}Sr_{0.4}Co_{0.5}Fe_{0.5}O_{3-\delta}$, that shows a much higher oxygen flux in the presence of pure CO_2 than the perovskite-type oxygen-transporting materials published so far. Furthermore, the $Pr_{0.6}Sr_{0.4}Co_{0.5}Fe_{0.5}O_{3-\delta}$ material was carefully tested in long-term permeation operations with pure He or pure CO_2 as the sweep gas on the permeate side of the membrane.

2. EXPERIMENTAL SECTION

Synthesis and Membrane Preparation. A powder sample of $Pr_{0.6}Sr_{0.4}Co_{0.5}Fe_{0.5}O_{3-\delta}$ (abbreviated as PSCF) was synthesized by a conventional one-pot sol–gel ethylenediaminetetraacetic acid (EDTA)/citric acid complexing method by mixing proper ratios of the metal nitrates with a total metal cation/EDTA/citric acid ratio of 1:1:1.5, as described elsewhere.[32] The as-synthesized powder was pressed into disks in a stainless steel module (18-mm i.d.) under a pressure of ~120 MPa that were then sintered at 1200 °C for 5 h in ambient air with heating/cooling rates of 2 °C min^{-1} to obtain disk membranes (approximately 0.6-mm thickness and 16-mm i.d.). The sintering time for the 1-mm-thick membrane was increased to 10 h under the same conditions.

X-ray Diffraction. The structural properties of the membranes were analyzed using X-ray diffraction (XRD) techniques. The data set was acquired at room temperature and in ambient air on a Bruker-AXS D8 Advance instrument with Cu K_α radiation in the step-scan mode within a 2θ range of 20–80° at 0.02° intervals. In situ XRD measurements between 30 and 1000 °C were conducted in an in situ cell HTK-1200 N (Anton-Paar) in an atmosphere consisting of 100 vol % CO_2 with a heating rate of 12 °C min^{-1} and an equilibrium time of 30 min prior to each measurement. The XRD data were analyzed using TOPAS 4.2 software (Bruker AXS).

Oxygen Permeation. The oxygen permeation flux was measured using a high-temperature permeation device schematically depicted in Figure 1. Freshly sintered disk membranes were sealed with gold paste (conducting paste C5754, Heraeus, Hanau, Germany) onto an alumina tube and positioned at the center of a vertical tubular oven. Synthetic air (20 vol % O_2/80 vol % N_2) at a flow of 150 cm^3 (STP) min^{-1} was applied to one side of the membrane, and the permeate side of the membrane was alternately swept with 50 cm^3 (STP) min^{-1} of He (Linde, 99.999%) and CO_2 (Linde, 99.5%). Mass flow controllers (MFCs) (Bronkhorst, Ruurlo, The Netherlands) were applied for all inlet gases, and the total effluent flow rate was measured with a soap-film flow meter. The quantitative analysis of the effluent mixture was performed using an online-coupled gas chromatograph (Agilent 6890A). Gas leakage through possible flaws in the sealing could be detected by monitoring the N_2 concentration in the effluent. The O_2 leakage could then be calculated and subtracted from the total O_2 flux.

dx.doi.org/10.1021/am501657j | ACS Appl. Mater. Interfaces 2014, 6, 10274–10282

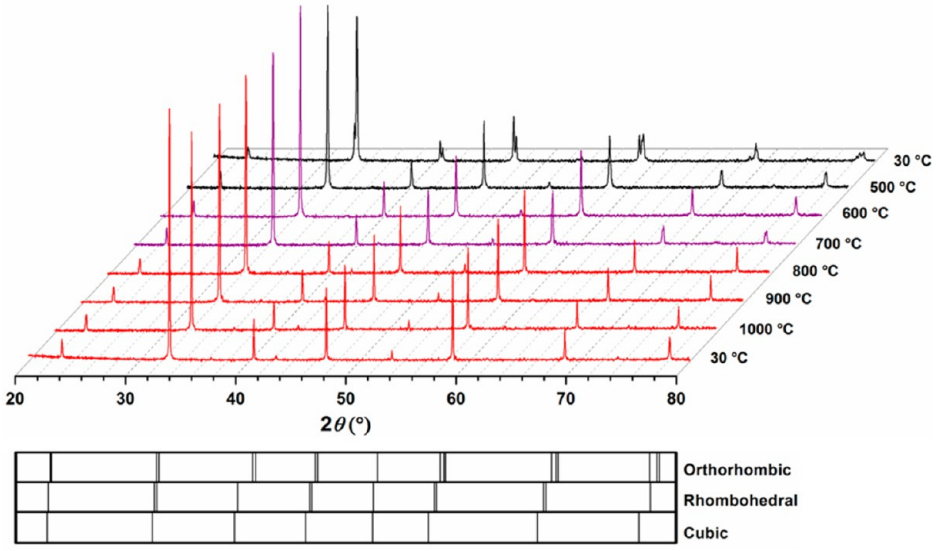

Figure 2. In situ XRD patterns of PSCF powder in an atmosphere of 100 vol % CO_2 at the given temperatures with the reflex positions of orthorhombic, rhombohedral, and cubic perovskite structures.

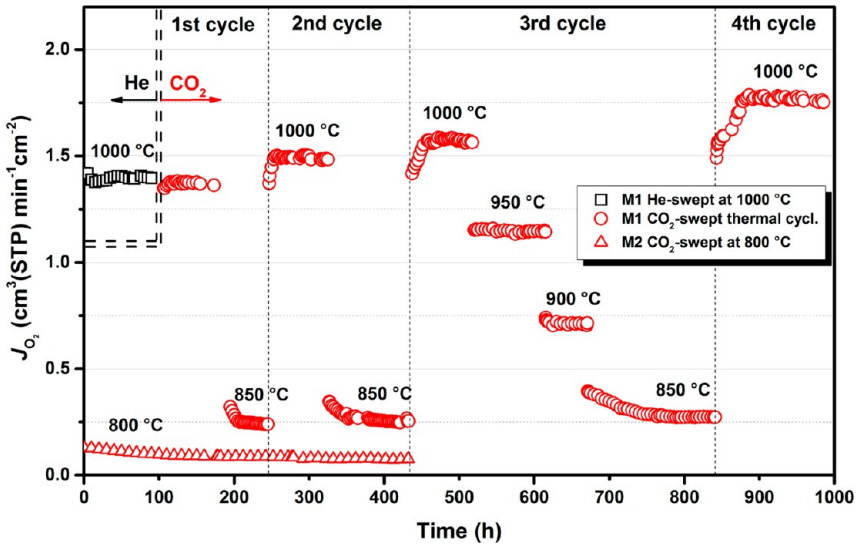

Figure 3. Oxygen permeation flux through PSCF disk membrane M1 with thermal cycling between 850 and 1000 °C and M2 at 800 °C. Sweep side M1: 50 cm^3 (STP) min^{-1} He (black squares)/CO_2 (red circles). Sweep side M2: 50 cm^3 (STP) min^{-1} CO_2 (red triangles). Feed side M1 and M2: 150 cm^3 (STP) min^{-1} synthetic air. Membrane thickness: 0.6 mm.

The initial oxygen permeation measurements on a 0.6-mm-thick PSCF membrane M1 were conducted with He as the sweep gas at 1000 °C. After a constant oxygen permeation flux was reached, the permeation fluxes were measured at varying temperatures in the following order: 1000, 950, 900, 850, and 800 °C. The measurements were continued for 100 h at 1000 °C, during which a constant permeation flux was maintained. The sweep gas was then switched to CO_2, and measurements were continued for 1000 h, during which the membrane was subjected to four thermal cycles as described in the next subsection. The heating/cooling rate was 2 °C min^{-1} for all temperature variations.

Thermal Cycling with CO_2 as the Sweep Gas. At 1000 °C, the system reached and maintained a constant oxygen flux after 80 h. The temperature was then lowered to 850 °C, and the oxygen flux was further measured. After 50 h at 850 °C with a stable oxygen flux, the second thermal cycle was started by ramping the temperature to 1000 °C. As in the first thermal cycle, the temperature was again lowered to 850 °C after a constant permeation level had been held for more than 100 h. Further oxygen permeation measurements were conducted for the third and fourth thermal cycles. After the oxygen flux had been measured at different temperatures (1000−800 °C) during the fourth thermal cycle, the temperature was again adjusted to 1000 °C, and the sweep gas was switched back to He. The oxygen permeation was then measured again at temperatures ranging from 1000 to 800 °C with He as the sweep gas.

Further long-term oxygen permeation measurements were conducted on 0.6-mm-thick PSCF membrane M2 at 800 °C with CO_2 sweeping for 450 h.

Scanning Electron Microscopy (SEM). The microstructures and surface morphologies of the membranes before and after the oxygen permeation measurements were studied using a field-emission scanning electron microscope of the type JEOL JSM-6700F at an excitation voltage of 2 kV. Energy-dispersive X-ray spectroscopy (EDXS) was employed using an Oxford Instruments INCA A-300 spectrometer at an excitation voltage of 20 kV to study the elemental distributions on the membrane's surface and within the grains.

3. RESULTS AND DISCUSSION

CO_2 Stability by in Situ XRD. The phase stability of PSCF was investigated using high-temperature in situ XRD measurements conducted on a powder sample in an atmosphere of 100 vol % CO_2 (Figure 2). An orthorhombic perovskite structure [space group *Imma* (No. 74)] exists at room temperature. Between 500 and 600 °C, a phase transition from orthorhombic to rhombohedral symmetry [space group $R\bar{3}c$ (No. 167)] occurs. The system undergoes a second phase transition to cubic perovskite symmetry [space group $Pm\bar{3}m$ (No. 221)] at 700−800 °C. It should be noted that, in an oxygen-free atmosphere, the cubic structure is maintained after the sample has been cooled to room temperature (Figure 2). However, during another in situ XRD measurement in an atmosphere of 50% CO_2 and 50% synthetic air, the initial orthorhombic symmetry was observed after the sample had been cooled to room temperature as a result of a declining oxygen vacancy concentration with decreasing temperature in an oxygen-containing atmosphere. The possible formation of $SrCO_3$ could not be confirmed from the in situ XRD results.

Oxygen Permeation. To investigate the membranes' CO_2 stability, long-term oxygen permeation measurements were conducted on two 0.6-mm-thick PSCF membranes with pure He (black squares) or pure CO_2 (red circles and triangles) as the sweep gas at different temperatures, as shown in Figure 3. Membrane M1 was stressed by rigorous thermal cycling, and the oxygen permeation flux was measured for both He and CO_2 as the sweep gases in the temperature range between 850 and 1000 °C. During the initial measurements at 1000 °C with He as the sweep gas, the PSCF membrane maintained a stable oxygen permeation flux of ∼1.38 cm^3 (STP) min^{-1} cm^{-2} for 100 h. Then, CO_2 was used as the sweep gas for the thermal cycling instead of He. During the first thermal cycle at 1000 °C, no significant decrease in permeation values was observed, and a constant permeation flux of 1.37 cm^3 (STP) min^{-1} cm^{-2} was measured for 80 h. Then, the temperature was gradually decreased from 1000 to 850 °C. At 850 °C, after a slow decrease in the oxygen permeation flux in the first 20 h, a steady state was reached, and a stable value of 0.25 cm^3 (STP) min^{-1} cm^{-2} was maintained for more than 50 h. This observation of a state with slowly decreasing fluxes followed by a steady state was also repeated in the following cycles (second and third cycles) at 850 °C. Moreover, from the first cycle to the third cycle, the duration of the state with decreasing fluxes increased from ca. 20 to ca. 100 h, and the oxygen permeation flux increased slightly from 0.25 to 0.27 cm^3 (STP) min^{-1} cm^{-2}. After the temperature had been increased from 850 to 1000 °C in the second, third, and fourth cycles, at the constant temperature of 1000 °C, a state of increasing fluxes and a steady state were clearly observed for each cycle. With increasing number of cycles, the duration of the state with increasing fluxes increased from ca. 10 to ca. 50 h, and the oxygen permeation flux increased clearly from 1.37 to 1.78 cm^3 (STP) min^{-1} cm^{-2}. The observation of a state of decreasing fluxes at 850 °C and a state of increasing fluxes at 1000 °C can be explained by carbonate formation at the grain boundaries at the lower temperature of 850 °C, followed by thermal decomposition at the higher temperature of 1000 °C, resulting in increased porosity of the membrane's surface on the CO_2-swept side, as shown in Figures 6 and 7. In addition to an increased surface area, the effect of a locally reduced membrane thickness due to grain depletion should not be overlooked. The observed holes varied in dimensions and were not uniformly distributed on the membrane surface, making it difficult to exactly determine the effect of the membrane's reduced thickness on the permeation flux. However, the observed depth of the local holes varied between 100 and 150 μm, which is obviously not sufficient to increase the permeation fluxes from 1.37 to 1.78 cm^3 (STP) min^{-1} cm^{-2}. Therefore, it can be concluded that the higher membrane surface area is the crucial factor for the increased oxygen permeation flux. The increased porosity of the membrane's surface on the CO_2-swept side can also explain the fact that, after each cycle, the system needed more time to achieve a steady state of oxygen permeation flux because increasing the membrane's surface area led to the formation of more carbonate and the higher amount of formed carbonate required a longer decomposition time at 1000 °C. It should be noted that the oxygen permeation flux maintained constant values of 0.74 and 1.18 cm^3 (STP) min^{-1} cm^{-2} during the whole time at 900 and 950 °C, respectively. It can be expected that the formation of carbonate on the PSCF membrane surface would not take place at 900 °C and above. It should also be considered that, according to the previously discussed in situ XRD results, no phase transitions were expected to occur in the temperature range of 850−1000 °C used for the thermal cycling and the perovskite-type cubic symmetry ($Pm\bar{3}m$) was maintained during each cycle. Possible phase transitions could have resulted in mechanical stresses across the membrane, thus leading to fractures and crack formation. The absence of cracks was verified by monitoring the concentration of N_2 in the effluent, which remained insignificant during the entire experiment.

Moreover, to investigate carbonate formation at lower temperatures, additional long-term oxygen permeation measurements were conducted on PSCF membrane M2 at 800 °C with pure CO_2 as the sweep gas. After the initial fast decrease of the oxygen permeation flux from 0.12 to 0.08 cm^3 (STP) min^{-1} cm^{-2} in the first 150 h at 800 °C, the oxygen permeation flux gradually reached a steady state after 300 h. This initial decrease of the oxygen concentration could be indicative of the local formation of $SrCO_3$ on the membrane's surface on the CO_2-swept side, which was further explored using SEM and EDX spectroscopy (Figures 5−11). The rate of $SrCO_3$ formation on the membrane surface is dependent on the concentration of Sr^{2+} on the membrane's surface layer, which decreases with the operation time at 800 °C. As a result, a steady state can be observed as the carbonate formation reaction ($Sr^{2+} + CO_3^{2-} \rightleftarrows SrCO_3$) is limited by very low amounts of Sr^{2+} on the membrane's surface layer.

Structure Characterization and Phase Stability. For the characterization of the PSCF membrane after long-term oxygen permeation measurements with 100 vol % CO_2 exposure on the sweep side at 1000 °C, X-ray diffraction (XRD) was applied on both feed and sweep sides of the spent membrane. The resulting XRD patterns measured at room temperature (Figure 4) indicate that the orthorhombic body-centered perovskite structure [space group *Imma* (No. 74)] of the freshly sintered PSCF membrane was maintained after the long-term oxygen permeation measurements with CO_2 as the sweep gas. No carbonate formation was evidenced, despite the fact that the A site of PSCF contains 40% alkaline-earth metal ion Sr^{2+} because the carbonate formed at the lower temperature of 850 °C was decomposed at the higher temperature of 1000 °C, before the sample was cooled to room temperature.

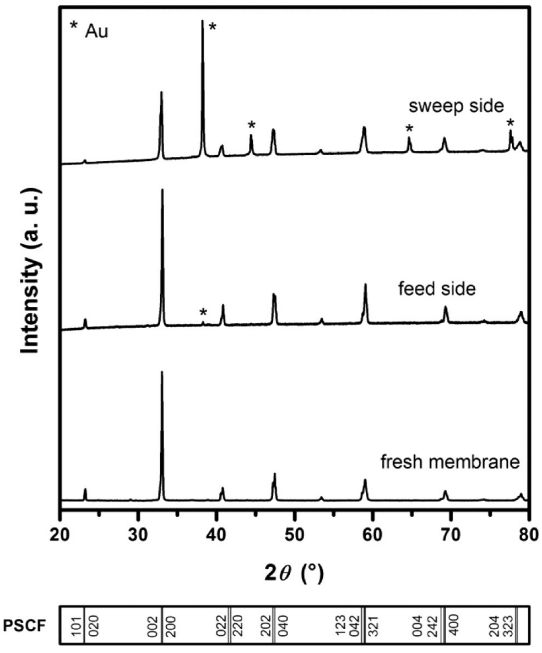

Figure 4. Room-temperature XRD patterns of freshly sintered PSCF membrane M1 (bottom), feed side of the spent membrane (middle), and sweep side of the membrane after 900 h of CO_2 exposure and 1000 h of long-term oxygen permeation operation (top). The reflex positions pertaining to gold from the sealing paste are marked with asterisks (*).

Microstructure and Elemental Analysis. The surface microstructure of the PSCF membranes before and after the long-term measurements with CO_2 sweeping was studied by SEM, as shown in Figures 5−7. The elemental distribution was

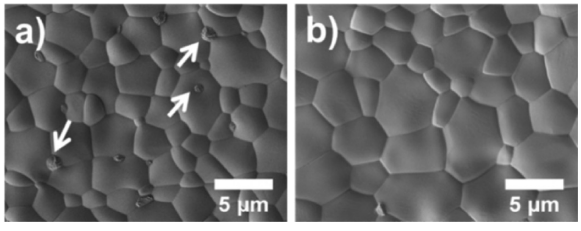

Figure 5. SEM micrographs of the PSCF membrane: (a) fresh membrane (cobalt oxide particles are marked with white arrows), (b) feed side of PSCF membrane M1 after long-term oxygen permeation operation with thermal cycling between 850 and 1000 °C.

studied by EDXS. The SEM micrographs of the fresh PSCF membrane show densely packed grains and a crack-free membrane surface (Figure 5a). However, some small particles could frequently be observed on the surface, which were found to be Co-rich particles (most probably cobalt oxide) using EDXS mapping. This observation of Co-rich particles was also found on the fresh $La_{0.6}Sr_{0.4}Co_{0.8}Fe_{0.2}O_{3-\delta}$ (LSCF) membrane by Klande et al.[24] Nonetheless, the elemental distribution throughout the membrane's surface and within the grains was homogeneous. After the long-term measurements for 1000 h, SEM micrographs of the feed/air side of PSCF membrane M1 showed no deterioration of the microstructure, and the Co-rich particles almost disappeared from the surface (Figure 5b). However, SEM micrographs of the membrane's cross section (Figure 6a) revealed a high occurrence of the local disintegration of grains on the sweep side of the membrane,

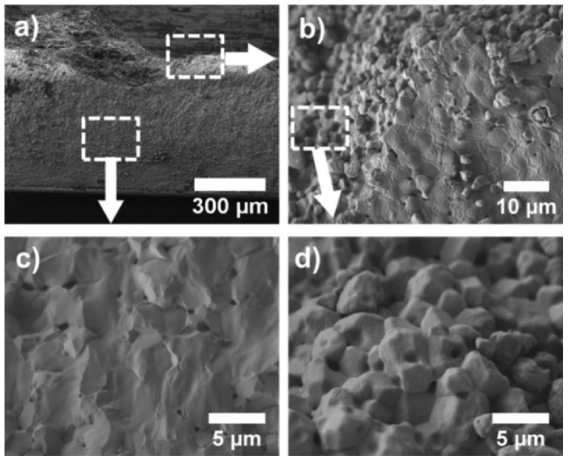

Figure 6. SEM micrographs of PSCF membrane M1 after long-term oxygen permeation operation with thermal cycling between 850 and 1000 °C: (a) membrane cross section, (b) formation of a flat hole as grains disintegrate from the permeate side, (c) cross section of the unchanged part in the middle of the membrane with densely packed grains and some closed porosity (black pinholes), (d) microstructure of the surface of the flat hole showing disintegrated grains.

which led to formation of several spots with alternating grain depletion (Figure 6b,d) and grain accumulation (Figure 7).

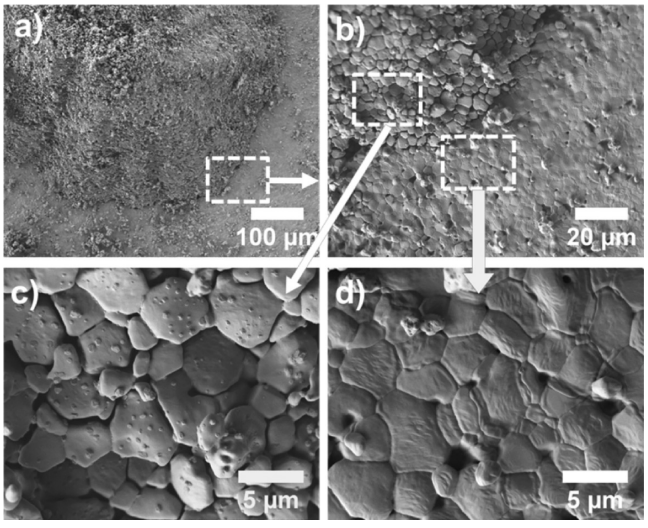

Figure 7. SEM micrographs of the permeate side of PSCF membrane M1 after long-term oxygen permeation operation with thermal cycling between 850 and 1000 °C: (a,b) local disintegration of the grains with different magnifications, (c) microstructure of the disintegrated grains, (d) unchanged part of the membrane with densely packed grains and some closed porosity (black pinholes).

This phenomenon could be caused by several thermal cycles with CO_2 sweeping. Long dwell times at 850 °C and below in the presence of 100 vol % CO_2 could have resulted in the formation of carbonates in the grain boundaries. The subsequent temperature rise at the end of each cycle should have then caused the decomposition of the formed carbonates, followed by the release of gaseous CO_2 from the grain boundaries, resulting in the local disintegration of grains from the membrane's surface and the formation of hills/valleys. The observation of the local accumulation of grains in the form of hills on the sweep side of the membrane was difficult to explain.

However, it is plausible that a mechanism similar to the primary nucleation stage during crystallization could be responsible for this phenomenon. Furthermore, no additional alteration of the microstructure could be detected in the inner depths of PSCF membrane M1 (Figure 6c). The formation of carbonates could not be verified by the in situ XRD results under pure CO_2 atmosphere at temperatures below 850 °C, which might be because the amount of the carbonate formed in the short dwell time was lower than the detection limit of the XRD instrument.

PSCF Membrane after 450 h of CO_2 Sweeping at 800 °C (M2). To investigate the CO_2 tolerance of the PSCF membrane at lower temperatures, a long-term oxygen permeation test was conducted on a PSCF membrane at 800 °C for 450 h of CO_2 sweeping, followed by SEM, EDXS, and XRD analyses. The SEM micrographs and the related elemental EDXS mappings of the sweep side and of the membrane's cross section close to the sweep side are depicted in Figures 8 and 9,

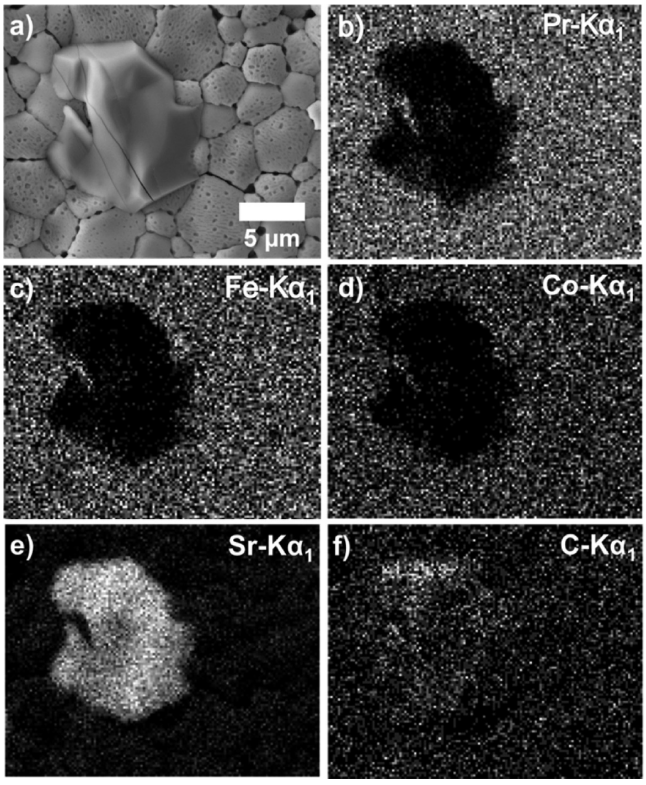

Figure 8. (a) SEM micrograph of the sweep side of PSCF membrane M2 after 450 h of CO_2 sweeping at 800 °C, (b–f) elemental distributions by EDXS of the area shown in panel a.

respectively. As expected, no alteration of the microstructure was observed on the feed side of the membrane. However, SEM imaging of the CO_2-swept permeate side revealed several spots where local formation of a second phase had occurred on top of the membrane's surface. Furthermore, numerous pores were formed at the grain boundaries, frequently resulting in dislocation of the grains. The EDXS analysis of the membrane's surface indicated that the extra phase was rich in Sr and C, as shown in Figure 8e,f. A closer inspection of the Sr distribution depicted in Figure 8e confirms the relative Sr depletion from the grain boundaries. However, no interconnecting cracks were observed, which was also in accordance with the absence of N_2 leakage in the gas chromatographs. The EDXS mapping of the membrane's cross section shows that the Sr-rich layer was

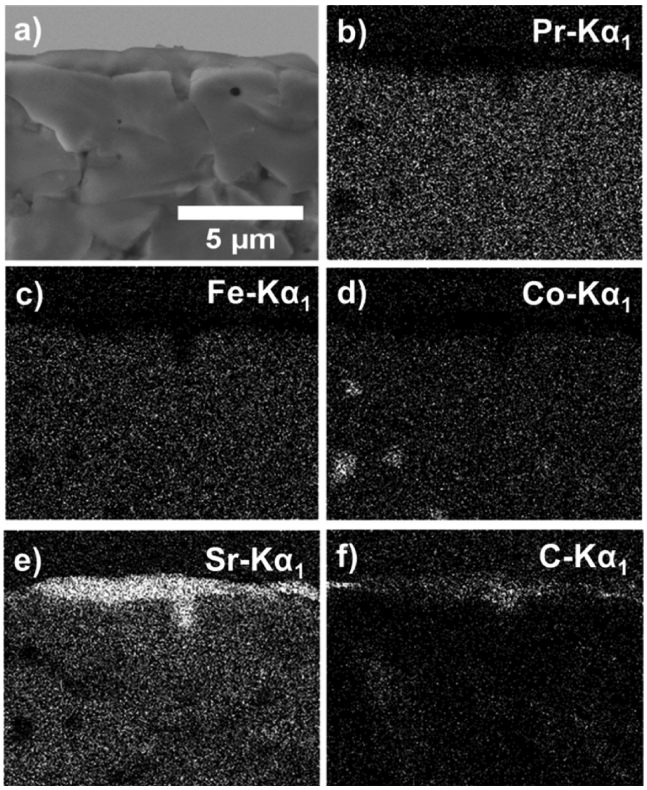

Figure 9. (a) SEM micrograph of PSCF membrane M2 cross section close to the permeate side after 450 h of CO_2 sweeping at 800 °C, (b–f) elemental distributions by EDXS of the area shown in panel a.

approximately 1–2 μm thick (Figure 9a). The formation of carbonates at 800 °C resulted in a decline in the oxygen permeation flux in the long run. However, it can be observed from Figure 3 that, after 150 h of slowly decreasing fluxes, a steady state was reached for at least 300 h. The existence of a micrometer-thick continuous carbonate layer was previously observed by Arnold et al.[17] and Klande et al.[24] In the case of the PSCF membrane, several isolated patches of $SrCO_3$ were formed on the membrane's surface. Furthermore, several Co-rich spots were detected, which were most probably cobalt oxide particles. The remaining elements, namely, Pr, Sr, and Fe, were homogeneously distributed. The presence of $SrCO_3$ could also be verified by the subsequent XRD measurements at room temperature on the spent PSCF M2 membrane (Figure 10).

PSCF Membrane after 300 h of CO_2 Sweeping at 950 °C (M3). To investigate the effect of CO_2 on the microstructure of the PSCF membrane, an additional test on PSCF membrane M3 was performed using CO_2 as the sweep gas at 950 °C for 300 h. After this test, the microstructure of the surface of the PSCF membrane M3 on the sweep side was characterized by SEM, and room-temperature XRD measurements were conducted to investigate the carbonate formation on the surface. The XRD patterns of PSCF membranes M2 and M3 and the corresponding SEM micrographs of their CO_2-swept sides are depicted in Figure 10. Although the formation of small amounts of carbonate on membrane M2 (after long-term CO_2 sweeping at 800 °C) is obvious, no carbonate formation on the M3 membrane surface was observed. In addition, no local disintegration of grains on the membrane surface on the sweep side of membrane M3 was observed in the SEM micrograph. In addition, the SEM micrograph of membrane M2 clearly exhibits pore formation at the grain boundaries due to strontium

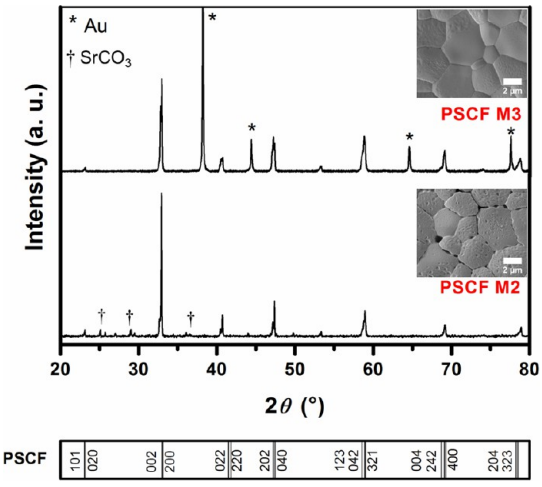

Figure 10. Top: Room-temperature XRD patterns of spent PSCF membranes M2 and M3 after long-term oxygen permeation operation with related SEM images. The reflex positions of gold from the gold paste and the formed $SrCO_3$ are marked with asterisks (*) and daggers (†), respectively.

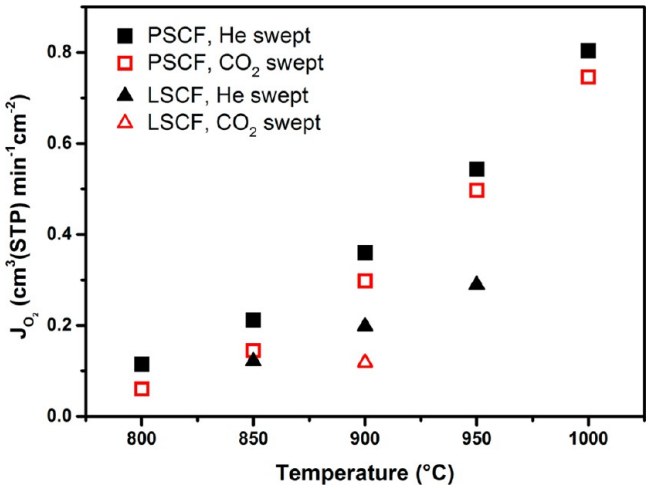

Figure 11. Temperature-dependent oxygen permeation fluxes of 1-mm-thick PSCF (square) and LSCF (triangle) disk membranes. Feed side: 150 cm^3 (STP) min^{-1} of synthetic air. Sweep side for PSCF: 50 cm^3 (STP) min^{-1} flow rate of He (solid) and CO_2 (open). The oxygen partial pressure gradient $[\ln(P_{O_2,feed}/P_{O_2,permeate})]$ across the PSCF membrane at 950 °C was 2.894 with He as the sweep gas. Sweep side for LSCF: 30 cm^3 (STP) min^{-1} flow of He (solid) and CO_2 (open). The oxygen partial pressure gradient across the LSCF membrane at 950 °C was 2.996 with He as the sweep gas.[24]

depletion, as was previously confirmed by EDXS analysis (Figure 8). The EDX mapping of the elements on the sweep side of membrane M3 also confirms a homogeneous elemental distribution and no detectable carbonate formation. By combining the results of the long-term operation of PSCF membrane M1 at 900 °C with constant fluxes during the third thermal cycle and no carbonate formation on the surface of PSCF membrane M3 at 950 °C, it can be deduced that the PSCF membrane exhibits an excellent stability in CO_2 at 900 °C and above.

Comparison of the Oxygen Permeabilities of PSCF and LSCF Membranes. The comparative results of oxygen permeation measurements conducted on the 1-mm-thick PSCF membrane and the previously reported $La_{0.6}Sr_{0.4}Co_{0.8}Fe_{0.2}O_{3-\delta}$ (LSCF)[24] membrane with the same thickness are shown in Figure 11. As can be seen, our PSCF perovskite membrane provided higher permeation fluxes than the LSCF perovskite membrane, which also had 40% Sr on the A site. For instance, at 950 °C, the PSCF membrane exhibited an oxygen permeation flux of 0.54 cm^3 (STP) min^{-1} cm^{-2}, which was slightly higher than the 0.30 cm^3 (STP) min^{-1} cm^{-2} value measured on the LSCF membrane with the same sweep gas (He). It should be noted that, at a lower temperature of 850 °C, the PSCF membrane had a higher permeation flux in an air/CO_2 oxygen gradient in comparison to the LSCF membrane in an air/He oxygen gradient. Nevertheless, in terms of CO_2 stability, the LSCF membrane also exhibited a good tolerance in CO_2 atmosphere after more than 200 h of operation at 900 °C,[24] which was similar to the tolerance of our PSCF membrane.

It is expected from the ionic radii of Pr^{3+} (132 pm) and La^{3+} (136 pm)[26] that replacing Sr^{2+} (144 pm) with Pr should result in a smaller unit cell than replacing Sr^{2+} with La. Nevertheless, the data analysis of the in situ XRD measurements shows a negligible difference in lattice parameters of the cubic perovskite structures at 1000 °C, with 39.3 and 39.4 pm for PSCF and LSCF, respectively.[24] However, from a steric point of view, doping the A site with a smaller rare-earth cation could increase the oxygen-ion mobility in the cubic perovskite lattice, which is in accordance with the geometric calculations of Kilner and Brook on $LnAlO_3$ systems (Ln = lanthanides), predicting a slight decrease in the oxygen migration enthalpies with decreasing dopant (here, rare-earth metal) ionic radius, for a fixed B-site composition.[33] In the comparative case of LSCF and PSCF, both materials contain 40 at. % Sr at the A site of the perovskite. However, the smaller ionic radius of Pr compared to La could facilitate oxygen-ion migration through the saddle-point configuration (the triangle of two A-site and one B-site cations), according to various studies.[28,33,34] Furthermore, it should be noted that Pr can simultaneously exist in the two valence states of Pr^{3+} and Pr^{4+} in its oxide form,[35] whereas La^{3+}, with the highest fourth ionization energy among lanthanides and the xenon noble-gas electron configuration, maintains its trivalent oxidation state.[36] The concurrence of different valence states of Pr^{3+} and Pr^{4+} could also be beneficial to the dissociation and reduction of molecular oxygen on the membrane's surface. Furthermore, Ishihara et al. reported high dissociation rates of molecular oxygen into ionic oxygen, which might be related to the facile redox cycle of Pr^{4+}/Pr^{3+} in $Pr_{0.6}Sr_{0.4}MnO_3$,[37] thus contributing to faster surface-exchange kinetics, when considering the dissociation of molecular oxygen at a Pr-terminated surface as in the following reaction using Kröger–Vink notation

$$Pr_{Pr}^{\times}V_O^{\bullet\bullet}Pr_{Pr}^{\times} + \frac{1}{2}O_2 \rightarrow Pr_{Pr}^{\bullet}O_O^{\times}Pr_{Pr}^{\bullet} \quad (1)$$

where $Pr_{Pr}^{\times}$ and $Pr_{Pr}^{\bullet}$ are Pr^{3+} and Pr^{4+}, respectively, and $V_O^{\bullet\bullet}$ is an oxygen vacancy.

4. CONCLUSIONS

The perovskite-type mixed-oxide conductor $Pr_{0.6}Sr_{0.4}Co_{0.5}Fe_{0.5}O_{3-\delta}$ was successfully prepared by a conventional sol–gel citric acid/EDTA complexing method. In situ XRD measurements revealed a structure transition from orthorhombic perovskite symmetry to rhombohedral symmetry at 500–600 °C and a second phase transition from

rhombohedral to cubic at 700−800 °C. In comparison with the extensively studied $La_{0.6}Sr_{0.4}Co_{0.8}Fe_{0.2}O_{3-\delta}$ (LSCF) materials under similar conditions, the PSCF membrane shows higher permeation fluxes because of the smaller ionic radius of the Pr^{3+} cation, which can decrease the potential energy barrier of oxygen migration. The fact that Pr can simultaneously exist in two valence states, Pr^{3+} and Pr^{4+}, not only could facilitate oxygen migration in the lattice from a steric perspective, but also could enhance the dissociation rate of molecular oxygen into ionic oxygen. A series of long-term oxygen permeation studies and chemical stability tests conducted on PSCF membranes showed that the PSCF membrane exhibits an excellent CO_2 tolerance and a high oxygen permeation performance at 900 °C and above, which suggests that PSCF can be considered as a promising candidate for applications in chemical processes involving the oxyfuel concept for CO_2 capture in this temperature range.

AUTHOR INFORMATION

Corresponding Author

*E-mail: kaveh.partovi@pci.uni-hannover.de. Tel.: +49-511-762-2125. Fax: +49-511-762-3175.

Notes

The authors declare no competing financial interest.

ACKNOWLEDGMENTS

The authors gratefully acknowledge financial support from the Sino-German Centre for Research Promotion (GZ676 and GZ911).

REFERENCES

(1) Dyer, P. N.; Richards, R. E.; Russek, S. L.; Taylor, D. M. Ion Transport Membrane Technology for Oxygen Separation and Syngas Production. *Solid State Ionics* **2000**, *134*, 21−33.

(2) Liang, F. Y.; Caro, J. Perovskite Membranes for High Temperature Oxygen Separation. In *Membrane Engineering for the Treatment of Gases*; Drioli, E., Barbieri, G., Eds.; Royal Society of Chemistry: London, 2011; Vol. 2, pp 192−221.

(3) Lin, Y. S.; Zeng, Y. Catalytic Properties of Oxygen Semipermeable Perovskite-Type Ceramic Membrane Materials for Oxidative Coupling of Methane. *J. Catal.* **1996**, *164*, 220−231.

(4) Jiang, H. Q.; Cao, Z. W.; Schirrmeister, S.; Schiestel, T.; Caro, J. A Coupling Strategy to Produce Hydrogen and Ethylene in a Membrane Reactor. *Angew. Chem., Int. Ed.* **2010**, *49*, 5656−5660.

(5) Caro, J.; Caspary, K. J.; Hamel, C.; Hoting, B.; Koelsch, P.; Langanke, B.; Nassauer, K.; Schiestel, T.; Schmidt, A.; Schomaecker, R.; Seidel-Morgenstern, A.; Tsotsas, E.; Voigt, I.; Wang, H.; Warsitz, R.; Werth, S.; Wolf, A. Catalytic Membrane Reactors for Partial Oxidation Using Perovskite Hollow Fiber Membranes and for Partial Hydrogenation Using a Catalytic Membrane Contactor. *Ind. Eng. Chem. Res.* **2007**, *46*, 2286−2294.

(6) Jiang, H. Q.; Wang, H. H.; Liang, F. Y.; Werth, S.; Schiestel, T.; Caro, J. Direct Decomposition of Nitrous Oxide to Nitrogen by in Situ Oxygen Removal with a Perovskite Membrane. *Angew. Chem., Int. Ed.* **2009**, *48*, 2983−2986.

(7) Balachandran, U.; Dusek, J. T.; Mieville, R. L.; Poeppel, R. B.; Kleefisch, M. S.; Pei, S.; Kobylinski, T. P.; Udovich, C. A.; Bose, A. C. Dense Ceramic Membranes for Partial Oxidation of Methane to Syngas. *Appl. Catal. A* **1995**, *133*, 19−29.

(8) Shao, Z. P.; Haile, S. M. A High-Performance Cathode for the Next Generation of Solid-Oxide Fuel Cells. *Nature* **2004**, *431*, 170−173.

(9) Huang, K.; Wan, J.; Goodenough, J. B. Oxide-Ion Conducting Ceramics for Solid Oxide Fuel Cells. *J. Mater. Sci.* **2001**, *36*, 1093−1098.

(10) Liang, F. Y.; Luo, H. X.; Partovi, K.; Ravkina, O.; Cao, Z. W.; Liu, Y.; Caro, J. A Novel CO_2-Stable Dual Phase Membrane with High Oxygen Permeability. *Chem. Commun.* **2014**, *50*, 2451−2454.

(11) Luo, H. X.; Efimov, K.; Jiang, H. Q.; Feldhoff, A.; Wang, H. H.; Caro, J. CO_2-Stable and Cobalt-Free Dual-Phase Membrane for Oxygen Separation. *Angew. Chem., Int. Ed.* **2011**, *50*, 759−763.

(12) Zhu, X.; Liu, H.; Cong, Y.; Yang, W. Novel Dual-Phase Membranes for CO_2 Capture via an Oxyfuel Route. *Chem. Commun.* **2012**, *48*, 251−253.

(13) Bouwmeester, H. J. M.; Burggraaf, A. J. Dense Ceramic Membranes for Oxygen Separation. In *Fundamentals of Inorganic Membrane Science and Technology*; Burggraaf, A. J.; Cot, L., Eds.; Elsevier Science B. V.: Amsterdam, The Netherlands, 1996; Vol. 4, Chapter 10, pp 435−528.

(14) Efimov, K.; Arnold, M.; Martynczuk, J.; Feldhoff, A. Crystalline Intermediate Phases in the Sol-Gel-Based Synthesis of $La_2NiO_{4+\delta}$. *J. Am. Ceram. Soc.* **2009**, *92*, 876−880.

(15) Liang, F. Y.; Jiang, H. Q.; Luo, H. X.; Caro, J.; Feldhoff, A. Phase Stability and Permeation Behavior of a Dead-End $Ba_{0.5}Sr_{0.5}Co_{0.8}Fe_{0.2}O_{3-\delta}$. *Chem. Mater.* **2011**, *23*, 4765−4772.

(16) ten Elshof, J. E.; Bouwmeester, H. J. M.; Verweij, H. Oxygen Transport through $La_{1-x}Sr_xFeO_{3-\delta}$. *Solid State Ionics* **1996**, *89*, 81−92.

(17) Arnold, M.; Wang, H.; Feldhoff, A. Influence of CO_2 on the Oxygen Permeation Performance and the Microstructure of Perovskite-Type $(Ba_{0.5}Sr_{0.5})(Co_{0.8}Fe_{0.2})O_{3-\delta}$. *J. Membr. Sci.* **2007**, *293*, 44−52.

(18) Czuprat, O.; Arnold, M.; Schirrmeister, S.; Schiestel, T.; Caro, J. Influence of CO_2 on the Oxygen Permeation Performance of Perovskite-Type $BaCo_xFe_yZr_zO_{3-\delta}$. *J. Membr. Sci.* **2010**, *364*, 132−137.

(19) Kharton, V. V.; Kovalevsky, A. V.; Viskup, A. P.; Figueiredo, F. M.; Yaremchenko, A. A.; Naumovich, E. N.; Marques, F. M. B. Oxygen Permeability of $Ce_{0.8}Gd_{0.2}O_{2-\delta}$−$La_{0.7}Sr_{0.3}MnO_{3-\delta}$ Composite Membranes. *J. Electrochem. Soc.* **2000**, *147*, 2814−2821.

(20) Chen, W.; Chen, C.; Winnubst, L. Ta-Doped $SrCo_{0.8}Fe_{0.2}O_{3-\delta}$ Membranes: Phase Stability and Oxygen Permeation in CO_2 Atmosphere. *Solid State Ionics* **2011**, *196*, 30−33.

(21) Zeng, Q.; Zuo, Y.; Fan, C.; Chen, C. CO_2-Tolerant Oxygen Separation Membranes Targeting CO_2 Capture Application. *J. Membr. Sci.* **2009**, *335*, 140−144.

(22) Sunarso, J.; Baumann, S.; Serra, J. M.; Meulenberg, W. A.; Liu, S.; Lin, Y. S.; da Costa, J. C. D. Mixed Ionic-Electronic Conducting (MIEC) Ceramic-Based Membranes for Oxygen Separation. *J. Membr. Sci.* **2008**, *320*, 13−41.

(23) Efimov, K.; Klande, T.; Juditzki, N.; Feldhoff, A. Ca-Containing CO_2-Tolerant Perovskite Materials for Oxygen Separation. *J. Membr. Sci.* **2012**, *389*, 205−215.

(24) Klande, T.; Ravkina, O.; Feldhoff, A. Effect of A-Site Lanthanum Doping on the CO_2 Tolerance of $SrCo_{0.8}Fe_{0.2}O_{3-\delta}$ Oxygen-Transporting Membranes. *J. Membr. Sci.* **2013**, *437*, 122−130.

(25) Yokokawa, H.; Sakai, N.; Kawada, T.; Dokiya, M. Thermodynamic Stabilities of Perovskite Oxides for Electrodes and Other Electrochemical Materials. *Solid State Ionics* **1992**, *52*, 43−56.

(26) Shannon, R. D. Revised Effective Ionic Radii and Systematic Studies of Interatomic Distances in Halides and Chalcogenides. *Acta Crystallogr. A: Cryst. Phys., Diffr., Theor. Gen. Crystallogr.* **1976**, *32*, 751−767.

(27) Tan, X.; Liu, N.; Meng, B.; Sunarso, J.; Zhang, K.; Liu, S. Oxygen Permeation Behavior of $La_{0.6}Sr_{0.4}Co_{0.8}Fe_{0.2}O_3$ Hollow Fibre Membranes with Highly Concentrated CO_2 Exposure. *J. Membr. Sci.* **2012**, *389*, 216−222.

(28) Teraoka, Y.; Nobunaga, T.; Yamazoe, N. Effect of Cation Substitution on the Oxygen Semipermeability of Perovskite-Type Oxides. *Chem. Lett.* **1988**, 503−506.

(29) Serra, J. M.; Vert, V. B.; Betz, M.; Haanappel, V. A. C.; Meulenberg, W. A.; Tietz, F. Screening of A-Substitution in the System $A_{0.68}Sr_{0.3}Fe_{0.8}Co_{0.2}O_{3-\delta}$ for SOFC Cathodes. *J. Electrochem. Soc.* **2008**, *155*, B207−B214.

(30) Luo, H. X.; Jiang, H. Q.; Klande, T.; Cao, Z. W.; Liang, F. Y.; Wang, H. H.; Caro, J. Novel Cobalt-Free, Noble Metal-Free Oxygen-

Permeable $40Pr_{0.6}Sr_{0.4}FeO_{3-\delta}$–$60Ce_{0.9}Pr_{0.1}O_{2-\delta}$ Dual-Phase Membrane. *Chem. Mater.* **2012**, *24*, 2148–2154.
(31) Liang, F. Y.; Luo, H. X.; Partovi, K.; Ravkina, O.; Cao, Z. W.; Yi, L.; Caro, J. A Novel CO_2-Stable Dual Phase Membrane with High Oxygen Permeability. *Chem. Commun.* **2014**, *50*, 2451–2454.
(32) Liang, F. Y.; Partovi, K.; Jiang, H. Q.; Luo, H. X.; Caro, J. B-Site La-Doped $BaFe_{0.95-x}La_xZr_{0.05}O_{3-\delta}$ Perovskite-Type Membranes for Oxygen Separation. *J. Mater. Chem. A* **2013**, *1*, 746–751.
(33) Kilner, J. A.; Brook, R. J. A Study of Oxygen Ion Conductivity in Doped Non-Stoichiometric Oxides. *Solid State Ionics* **1982**, *6*, 237–252.
(34) Cherry, M.; Islam, M. S.; Catlow, C. R. A. Oxygen Ion Migration in Perovskite-Type Oxides. *J. Solid State Chem.* **1995**, *118*, 125–132.
(35) Borchert, Y.; Sonstrom, P.; Wilhelm, M.; Borchert, H.; Baumer, M. Nanostructured Praseodymium Oxide: Preparation, Structure, and Catalytic Properties. *J. Phys. Chem. C* **2008**, *112*, 3054–3063.
(36) Lang, F.; Smith, B. C. Ionization Energies of Lanthanides. *J. Chem. Educ.* **2010**, *87*, 875–881.
(37) Ishihara, T.; Kudo, T.; Matsuda, H.; Takita, Y. Doped $PrMnO_3$ Perovskite Oxide as a New Cathode of Solid Oxide Fuel Cells for Low Temperature Operation. *J. Electrochem. Soc.* **1995**, *142*, 1519–1524.